Conference on Modelling Fluid Flow (CMFF'22)
The 18th International Conference on Fluid Flow Technologies
Budapest, Hungary, August 30-September 2, 2022

Direct Numerical Simulation of Shallow Water Breaking Waves Generated by Wave Plate

Shuo LIU[1], Hui WANG[2], Annie-Claude BAYEUL-LAINÉ[3], Olivier COUTIER-DELGOSHA[4]

[1] Corresponding Author. Univ. Lille, CNRS, ONERA, Arts et Métiers Institute of Technology, Centrale Lille, UMR 9014 – LMFL – Laboratoire de Mécanique des Fluides de Lille – Kampé de Fériet, F-59000, Lille, France. Tel.: +33 784 539 404, E-mail: shuo.liu@ensam.eu
[2] Univ. Lille, CNRS, ONERA, Arts et Métiers Institute of Technology, Centrale Lille, UMR 9014 – LMFL – Laboratoire de Mécanique des Fluides de Lille – Kampé de Fériet, F-59000, Lille, France. E-mail: hui.wang@ensam.eu
[3] Univ. Lille, CNRS, ONERA, Arts et Métiers Institute of Technology, Centrale Lille, UMR 9014 – LMFL – Laboratoire de Mécanique des Fluides de Lille – Kampé de Fériet, F-59000, Lille, France. E-mail: annie-claude.bayeul-laine@ensam.eu
[4] Univ. Lille, CNRS, ONERA, Arts et Métiers Institute of Technology, Centrale Lille, UMR 9014 – LMFL – Laboratoire de Mécanique des Fluides de Lille – Kampé de Fériet, F-59000, Lille, France. E-mail: olivier.coutier-delgosha@ensam.eu

ABSTRACT

We present a two-dimensional direct numerical simulation of breaking waves in shallow water generated by a wave plate. The open-source Basilisk solver is used to solve the incompressible, variable-density, two-phase Navier-Stokes equations with surface tension. The air-water interface is advected using a momentum-conservative Volume-of-Fluid (MCVOF) scheme. The surface tension is treated with a balanced-force technique. An Adaptive Mesh Refinement (AMR) scheme is employed for computational efficiency, concentrating computational resources on significant solution regions. By reconstructing the piston-type wave plate numerically, we realize a high-fidelity simulation of experimental waves under the wide-ranging motions of the wave plate. The relationship between varying maximum wave plate speeds and the associated maximum wave heights before breaking is investigated. The onset of wave breaking is determined as a function of the ratio of wave height to water depth to distinguish between non-breaking waves, spilling breakers, and plunging breakers. A typical plunging breaking wave with a large ratio of wave height to water depth is initialized to identify the wave breaking and air entrainment processes. We obtain a good collapse of the simulated free-surface evolution and velocity fields with respect to the experiment. The shape and size of the air entrapped at impact by the plunging jet match closely the experimental observations during wave breaking. The time-evolving energy budget and the bubble characteristics under breaking waves are further discussed based on the numerical results.

Keywords: air entrainment, direct numerical simulation, two-phase flow, wave breaking

NOMENCLATURE

E	$[J]$	energy
H	$[m]$	maximum wave height before breaking
S	$[m]$	wavemaker stroke length
ϵ	$[J/s]$	viscous dissipation rate
σ	$[N/m]$	surface tension coefficient
A	$[m^2]$	area of ingested bubbles
c	$[-]$	volume fraction
d	$[m]$	still water depth
f	$[s^{-}1]$	wavemaker frequency
L	$[m]$	numerical domain size
l	$[-]$	maximum level of refinement
$N(t)$	$[-]$	number of bubbles
p	$[Pa]$	pressure field
t_{im}	$[s]$	the time of jet impact
V_{max}	$[m/s]$	maximum wave plate velocity
$\underline{\underline{D}}$	$[-]$	deformation tensor
$\underline{f_\sigma}$	$[N/m^3]$	surface tension force per unit volume
$\underline{u}$	$[m/s]$	fluid velocity
μ	$[Pa\ s]$	dynamic viscosity
ρ	$[kg/m^3]$	fluid density

Subscripts and Superscripts

k, p, m, d	kinetic, potential, mechanical, and dissipative energy
x, z	streamwise, vertical direction
$1, 2$	phase 1, water; phase 2, air

1. INTRODUCTION

Wave breaking has sparked a lot of research interests due to its importance in upper ocean dynamics and air-sea interactions. The experimental investigations of breaking waves by Duncan [1] and Melville [2] have initiated the exploration of the physics governing their instability, breaking onset, and strength.

Progress has been made in several areas, including prediction of geometric properties, breaking onset, energy dissipation, and air entrainment mechanisms in breaking waves. The turbulence directly associated with breaking is dominant in mixing processes beneath the free surface, making it crucial for heat, mass, and momentum transfer [3]. However, splashing, turbulence, and air entrainment make theoretical modeling challenging once the wave breaks. In addition, field measurements using various detection methods have difficulty in quantifying wave breaking due to the strongly nonlinear intermittent breaking process and environmental influences [4]. Controlled laboratory experiments and numerical modelling enable the isolation and analysis of the effects of wave breaking on a variety of fundamental air-sea interfacial properties, measuring the scaling relationships between surface wave fields and the kinematics and dynamics of breaking waves [5, 6]. Measurements of breaking waves generated by wave plate can provide general entrainment processes visualized by high speed imaging and the temporal evolution of turbulence quantified using particle image velocimetry (PIV), but there are also many technical challenges in measuring the temporo-spatial evolution and resolving both the large and small structures simultaneously during wave breaking. Therefore, direct numerical simulation (DNS) has becomes a feasible method for solving complex breaking processes across a wide range of scales, allowing researchers to gain a better understanding of the physical role of entrained air bubbles in basic processes such as wave energy dissipation. The numerical methodology followed in this investigation involves the simulation of incompressible flow of two immiscible fluids. The Navier-Stokes equations are solved numerically on sufficiently fine grids to retain the effects of viscosity and surface tension, allowing the physical properties of breaking waves to be accurately captured.

2. NUMERICAL SCHEME

2.1. Basilisk Solver

We solve the gas-liquid two-phase incompressible Navier-Stokes equations with variable density and surface tension using the Basilisk library. The Basilisk package is an open-source program for the solution of a wide variety of partial differential equation systems on regular adaptive Cartesian meshes. The incompressible, variable density Navier-Stokes equations with surface tension can be written as:

$$\rho(\partial_t \boldsymbol{u} + (\boldsymbol{u} \cdot \nabla)\boldsymbol{u}) = -\nabla p + \nabla \cdot (2\mu \boldsymbol{D}) + \boldsymbol{f}_\sigma \tag{1}$$

$$\partial_t \rho + \nabla \cdot (\rho \boldsymbol{u}) = 0 \tag{2}$$

$$\nabla \cdot \boldsymbol{u} = 0 \tag{3}$$

With $\boldsymbol{u} = (u, v, w)$ the fluid velocity, $\rho \equiv \rho(x, t)$ the fluid density, p the pressure, $\mu \equiv \mu(x, t)$ the dynamic viscosity, D the deformation tensor defined as $D_{ij} \equiv (\partial_i u_j + \partial_j u_i)/2$, and f_σ the surface tension force per unit volume.

The liquid-gas interface is tracked by the momentum-conserving volume-of-fluid (MCVOF) advection scheme [7] combined with quad/octree adaptive mesh refinement (AMR) method, while the corresponding volume fraction field is solved by a piecewise-linear geometrical scheme [8] together with a balanced-force continuous-surface-force model for the surface tension. The generic time loop is used for the implementation of numerical scheme and the timestep is limited by the CFL condition. The momentum equation is projected using the Bell-Colella-Glaz advection scheme [9], and the viscous terms are solved implicitly. Gravity is taken into account using the "reduced gravity approach" [10].

2.2. Momentum-Conserving VOF Method

The VOF method was originally developed by Hirt & Nichols (1981) [11] and modified by Kothe *et al.* (1991) [12], and further coupled with momentum conservation by Fuster & Popinet (2018) [7], with the advantage of allowing variable spatial resolution and sharp representation along the interface, while limiting the appearance of spurious numerical parasitic currents caused by momentum leakage between the dense and light phases [13]. A function $c(x, t)$, defined as the volume fraction of a particular fluid in each cell of the computational mesh, assuming a value from 0 to 1 for each phase, is used to reconstruct the interface of the two-phase flow. The density and viscosity can thus be calculated using arithmetic means as follows:

$$\rho(c) = c\rho_1 + (1 - c)\rho_2 \tag{4}$$

$$\mu(c) = c\mu_1 + (1 - c)\mu_2 \tag{5}$$

with ρ_1, ρ_2, and μ_1, μ_2 the density and viscosity of the first and second fluids, respectively.

The advection equation for the density can be substituted with an equivalent advection equation for the volume fraction:

$$\partial_t c + \nabla \cdot (c\boldsymbol{u}) = 0 \tag{6}$$

The piecewise linear interface construction (PLIC) approach is applied. The interface normal is computed by the Mixed-Youngs-Centered (MYC) method [14] and the position of the interface in the cell is determined using the method of Scardovelli & Zaleski (2000) [15].

Momentum conserving scheme in the advective momentum fluxes near the interface has proven to be essential to reduce the numerical momentum transfer through the interface, especially for large density difference between the two phases. The total fluxes on each face are obtained by adding the diffusive flux due to the viscous term, which are computed by a semi-implicit Crank-Nicholson scheme. The Bell-Collela-Glaz (BCG) second-order upwind scheme is used to reconstruct the liquid and gas momentum per unit volume to be advected in the cell.

2.3. Balanced-Force Surface Tension

Surface tension can be important in capturing the main cavity at impact and wave hydrodynamics during the post-breaking process. Surface tension is treated with the method of Brackbill *et al.* (1992) [16] and the balanced-force technique [17] as further developed by Popinet (2009, 2018) [18, 19]. To solve the inconsistency at low interface resolution, a generalized version of the height-function (HF) curvature estimation is used, resulting in accurate and efficient surface-tension-driven flow solutions.

3. PROBLEM DESCRIPTION AND MODEL VALIDATION

3.1. Problem Description

A series of breaking wave experiments have been conducted at Johns Hopkins University in a $6m$ long, $0.3m$ wide, and $0.6m$ high wave flume with the aim to study the dispersion of oil spills by breaking waves [20, 21]. The breaking waves are initialized by driving a piston-type wavemaker over a uniform water depth $d = 0.25m$. A single wave breaking event is generated by a single push of the wavemaker, with a trajectory $x(t)$ and associated wave plate velocity $v(t)$ determined by the following functions:

$$x(t) = \frac{S}{2}(1 - \cos(2\pi f t)), 0 \leq t \leq \frac{1}{2f} \tag{7}$$

$$v(t) = S\pi f \sin(2\pi f t), 0 \leq t \leq \frac{1}{2f} \tag{8}$$

where S is the wavemaker stroke length, f is the frequency, and t is the time.

On the basis of the laboratory experiments, two-dimensional simulations of breaking waves have been performed using the Basilisk solver. A plunging breaking wave with $S = 0.5334m$ and $f = 0.75Hz$ is chosen for detailed study, with a maximum wave plate velocity of $V_{\max} = S\pi f = 1.26m/s$. A parametric study is carried out to relate the wave characteristics to the initial conditions by varying the stroke S and frequency f. We define x as the streamwise direction, and z as the vertical direction, positive upward and measured from the still water level. (see Figure 1).

A constant depth of water for the interface $\eta(x, z)_{(t=0)} = d$, with d the still water depth, is used as the initial condition in a square box of size $L = 6m$. The wave propagates from left to right in the x direction. Based on direct numerical simulations of water-air mixture resulting from the entrainment of bubbles

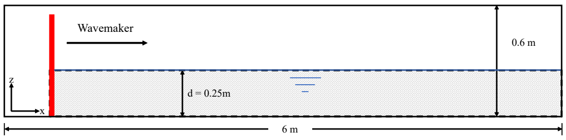

Figure 1. Sketch of laboratory breaking wave experiment and numerical domain.

due to breaking, we intend to investigate the mechanisms of breaking waves in terms of free-surface profiles, time-evolving energy budget and bubble characteristics.

3.2. Parameter Space

The density and viscosity ratios of the two phases are those of air and water in the experiments, which are $1.29/1018.3$ and $17.9e-6/1.01e-3$, respectively. The Reynolds number in the breaking waves generated by the wave plate can be defined by $Re = \rho V_{\max} S/\mu$, with ρ the density of water, $V_{\max}$ the maximum wave plate velocity, and S the stroke length [22]. The surface tension can be expressed by the Weber number $We = \rho V_{\max}^2 S/\sigma$, with σ the constant surface tension coefficient between water and air. The numerical resolution is given by $\Delta = L/2^l$, where l is the maximum level of refinement in the AMR scheme. The maximum level of refinement depends on the smallest particle size that needs to be resolved in the breaking waves. A maximum level of refinement of 15 is applied in this study, which corresponds to an equivalent conventional grid of 1 billion $((2^{15})^2)$ and a minimum mesh size of $122\mu m$. The grid is adaptively refined/coarsened as the wave propagates, resulting in a total number of grids ranging from 1 million to 10 million. The surface tension scheme is time-explicit, so the maximum timestep is the oscillation period of the smallest capillary wave. For the maximum level of refinement $l = 15$, the corresponding maximum timestep should not be larger than $6.4e-5$. To ensure numerical stability, we require the CFL number to be varied in accordance with the various stages of wave breaking evolution, generally decreasing from 0.5 to 0.3. The refinement criterion is based on the wavelet-estimated discretization error in terms of velocity, vorticity or VOF fields [23]. The refinement criteria on the VOF tracers and the velocity field components are used for adaptive refinement to capture the water-air interface and moving wave plate. The refinement algorithm is invoked at every timestep to determine whether to refine based on the criteria of wavelet estimated error $u_{\mathrm{err}} = 1e-3$ for velocity field and $f_{\mathrm{err}} = 1e-6$ for volume fraction field.

For a plunging breaking wave with $S = 0.5334m$ and $f = 0.75Hz$, due to the limitation of computational resources, combined with the decreasing effects of Reynolds number on the evolution of wave breaking, we choose $Re = 1 \times 10^5$. This value of Reynolds number corresponds to a maximum wave plate velocity of $0.51 m/s$ and a water depth of $0.08m$, which is 5-6 order of magnitude smaller than the actual value. We expect that Reynolds-number effects should not fundamentally alter the basic nature of the scaling we have derived [24]. The effect of surface tension on the formation of the main cavity is analyzed using the physical value of the surface tension coefficient between water and air $\sigma = 0.0728 kg/s^2$, which leads to $We = 12000$.

3.3. Breaking Waves Validation

3.3.1. Breaking waves profiles

Three high-speed cameras with a frame rate of 500 frames per second are used in the experiments to visualize the development of wave breaking and the subsequent breakup processes. The horizontal centers of the fields of view, 103×103, 75×75, and $75 \times 75 cm^2$, are located at $x = 1.66$, 2.43, and $3.07m$ for cameras 1, 2, and 3, respectively. The vertical center of all cameras are adjusted to the initial free surface. We compare numerical results of interface evolution over time for a plunging breaker generated by a motion of wave plate with $S = 0.5334m$ and $f = 0.75$ to the experimental snapshots taken with the high-speed cameras. Comparisons of the free surface profile between the simulation results and the snapshots taken during the experiments are shown in Figure 2.

Camera 1, located upstream of the wave direction, close to the side of the wave plate, is primarily responsible for recording the development of the plunging jet, the jet impact and air entrainment, and the generation of the first splash-up. As shown in Fig. 2(a) and Fig. 2(b), comparisons of the free surface evolution at $t = 0.6s$ and $0.7s$ show a great agreement between the present simulations and the experimental results from Camera 1. With the steepening of the wave slope and the curling of the wave crest, A plunging jet can be observed at $t = 0.6s$, with a tendency to project downward to the water surface. At $t = 0.7s$ the plunging jet impacts onto the rising wave front, forming the main cavity by entrapping a tube of air. During this process, the evolution of the free surface, including the development of the wave crest, the curvature of the overturning wave crest, the precise size of the main cavity, and the height and position of the first splash-up, can be accurately predicted by our numerical simulation.

The subsequent development of the initial wave crest and the first splash-up are recorded by Camera 2. From $t = 0.9s$ to $1.0s$, because of the propagation of the perturbations and capillaries at the main free surface prior to the impact of the first splash-up, the free surface beneath the ligaments and droplets of the first splash-up has already been disturbed (c). Following that, the first splash-up dives and connects to the free surface (d). The initial wave crest weakens, the main cavity expands and ruptures, generating a large number of small bubbles that then float to the vicinity of the free surface due to buoyancy. During

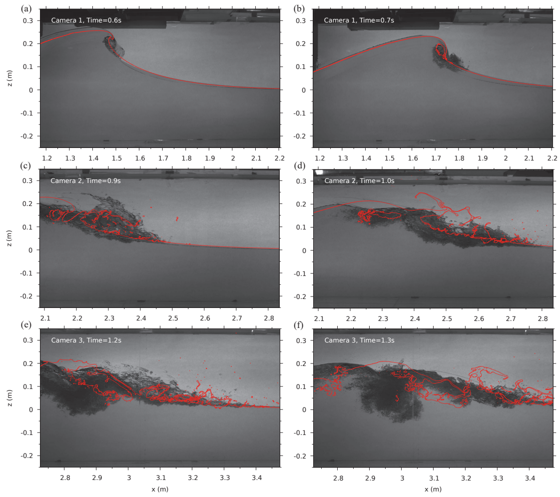

Figure 2. Comparison of free surface profile between laboratory images and numerical results

this process, more abundant water droplets and ligaments are observed in the experiment compared to our numerical results, as indicated by the black region in the experimental snapshots. The explanation for this is that our grid scale is fine enough to capture the formation of water droplets, air bubbles, and ligaments, but these phenomena can not be fully acquired using the present 2D numerical simulation.

Some differences are observed in the simulated free surface evolution compared to the snapshots taken by Camera 3. In comparison to the experimental observations, we find similar phenomena in the occurrence and rising of the second splash-up, as well as the decaying wave crest (e), but the exact development of the second splash-up and the rising wave front are not reproduced by our numerical simulation. It appears to be a phase shift in the distribution of the bubble cloud region (f), but similar bubble cloud size and penetration depth under the water can be obtained. These discrepancies can be explained by the fact that a slight perturbation at the wave front eventually leads to the development of drastically different breaking processes, and this chaotic behavior of breaking waves has been investigated across several runs with the same laboratory setup, demonstrating a non-repeatable breaking process particularly in the post-breaking region [25].

To sum up briefly, a good agreement is obtained in terms of wave shape and maximum wave height before breaking, and the simulated size of the main cavity entrapped by the plunging jet is almost the same compared to the experiment. Some differences can be seen in the location after wave breaking. The generation of water droplets, air bubbles, and ligaments is inaccurate, the profiles of the wave front and the distribution of bubble cloud region can not be well reproduced. This can be explained by the lack of bubbles and droplets generation due to the absence of 3D effects, and the chaotic behavior of

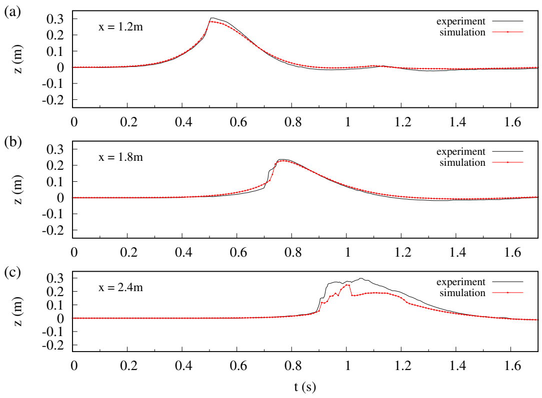

Figure 3. Comparison of surface elevations over time at x = 1.2m (a), 1.8m (b), and 2.4m (c)

breaking waves in the post-breaking region.

3.3.2. Surface elevation over time

Figure 3. shows the simulated free-surface profiles over time recorded at three positions ($x = 1.2m$, $1.8m$, and $2.4m$) corresponding to the pre-breaking, breaking, and post-breaking regions, respectively, with a comparison to the experimental high-speed imaging results.

The free-surface profile at the first position ($x = 1.2m$) remains smoothly curved, which corresponds to the pre-breaking stage with a smooth free-surface, without the formation of vertical interface and the generation of bubbles and droplets (a). The numerical simulation accurately reproduces the evolution of the free surface, including the development of the rising and falling wave profile, with only a slight underestimation ($0.02m$, 6.7% error) at the peak of the wave profile at $t = 0.5s$.

The second position is located at $x = 1.8m$, within the wave breaking region, near the main cavity entrapped by the plunging jet. We notice that in the experiment, the free-surface appears an immediate rise after jet impact at around $t = 0.7s$, indicating the penetration of the plunging jet into the wave front and the formation of the main cavity. Fig. 3(b) shows that our numerical simulation can closely capture the phenomena during wave breaking. The only discrepancy can be attributed to the lack of the production of small splashes when the plunging jet penetrates into the wave front due to the absence of 3D effects.

The wave propagates to the third position and develops into turbulence, forming a large amount of droplets and bubbles. There are apparent fluctuations of the free-surface between $t = 0.9s$ and $1.4s$, showing the strongly turbulent phenomena during this period. Fig. 3(c) shows an overall underestimation in the elevation of the free surface from $t = 0.9s$ to $1.4s$ by our numerical simulation. This is most likely due to the fact that the free surface elevation is measured differently in the experiment than in the numerical simulation. The value of the free surface elevation in the experiment is the maximum elevation between the wave profile, the splashing bubbles and droplets, as the free surface elevation is recorded from the black region in the experimental snapshots. However, in the numerical simulation, the free surface elevation is primarily determined by the wave profile rather than the splashing droplets scattered above the water surface.

In general, the temporal evolution of the free-surface profile can be precisely reproduced by our simulation compared to the experimental measurements at each location. Despite the limitations of 2D simulation in producing droplets and ligaments in the spanwise direction, the ability of our model to capture wave hydrodynamics, including accurate reproduction of wave height, wave speed, and wave breaking processes, can be demonstrated through the above comparisons.

4. DISCUSSIONS

4.1. Relationship between Wave Height and Maximum Wave Plate Speed

We develop relationships to connect the maximum wave height before breaking H with the maximum wave plate speed used for generating our waves, which is $V_{\max} = A\pi f$ in this study. We restrict consideration to air-water systems close to standard temperature and pressure, so a constant surface tension coefficient is used here. The relationship between H and $V_{\max}$ has been investigated by conducting various cases with different $V_{\max}$. The influence of Reynolds number on the resulting wave height has also been examined by using distinct values of $Re = 10^5$ and $Re = 6 \times 10^5$.

Figure 4. illustrates the relationship between H and $V_{\max}$ normalized by water depth d and shallow water wave speed, $(gd)^{1/2}$, respectively. Experimental measurements performed by Li (2017) [20] are also plotted in this figure. It can be seen that the data collapses onto a single line. As $V_{\max}$ increases, the regular wave begins to break, and the breaking type changes from spilling to plunging. Compared to the experimental data, our numerical results underestimate the wave height, and the differences between them increase with $V_{\max}$. The assumption that the flow becomes independent of the Reynolds number for sufficiently large values of Re can be validated from here. The transitions between regular and breaking waves, spilling and plunging breakers take place at around $H/d = 0.65$ and $H/d = 0.80$, respectively. This is very close to the measurement done by Li (2017), which showed a critical value of $H/d = 0.8$ for spilling and plunging breakers.

A linear correlation between the maximum wave height before breaking H and the maximum wave plate speed $V_{\max}$ has been revealed, showing that the wave height becomes higher as the maximum wave speed increases. The approximate transitions are represented by two critical values. The resulting wave heights between two regimes with distinct Re values are quite consistent, indicating that the evolution

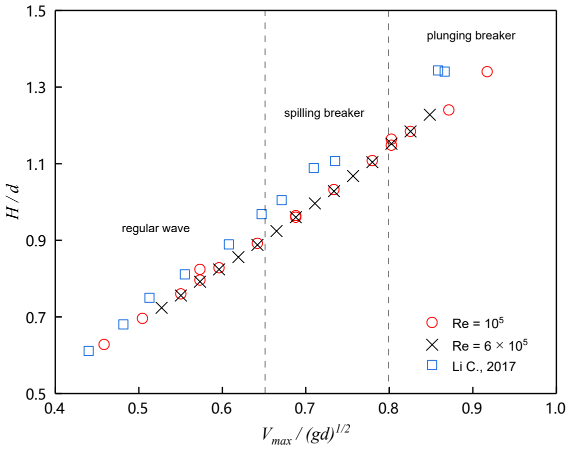

Figure 4. Relationship between maximum wave height before breaking H and maximum wave plate speed V_{max}

of the wave profiles over time is independent on the Reynolds number.

4.2. Energy Budget

We present an energy budget after the jet impact and analyze the energy decay and viscous dissipation due to breaking. The time histories of the kinetic E_{k}, potential E_{p} and total mechanical energy E_{m} are shown in Figure 5. The total mechanical energy of the wave is calculated as the sum of the kinetic and potential components $E_{\mathrm{m}} = E_{\mathrm{k}} + E_{\mathrm{p}}$. The Data are non-dimensionalized using initial values related to the jet impact time t_{im}.

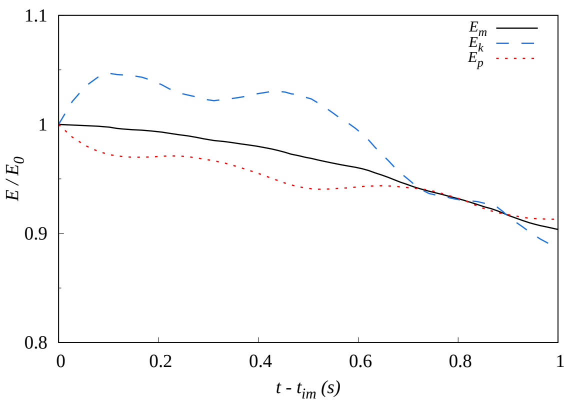

Figure 5. Time histories of the kinetic E_{k}, potential E_{p} and total mechanical energy E_{m}

Starting from the initial impact of the plunging jet, there are two visible energy transfers between kinetic and potential energies, leading to two apparent splash-up productions. As wave breaking develops, the wave crest diminishes, the plunging jet strikes the free surface and penetrates into the water, E_{k} rapidly increases and E_{p} begins to decline, until the first and second splash-ups occur at $t - t_{\mathrm{im}} = 0.1s$ and $t - t_{\mathrm{im}} = 0.45s$, respectively. When the splash-up starts to rise, E_{k}, which has reached its maximum, begins to decline and transfers to potential energy. The total energy decays gradually with a continuously increasing decay rate during this breaking phase. In the later stage of breaking waves, notably after $t - t_{\mathrm{im}} = 0.65s$, the wave becomes more turbulent, and the total mechanical energy exhibits a greater decay due to the substantial air-water mixtures and vortical structures.

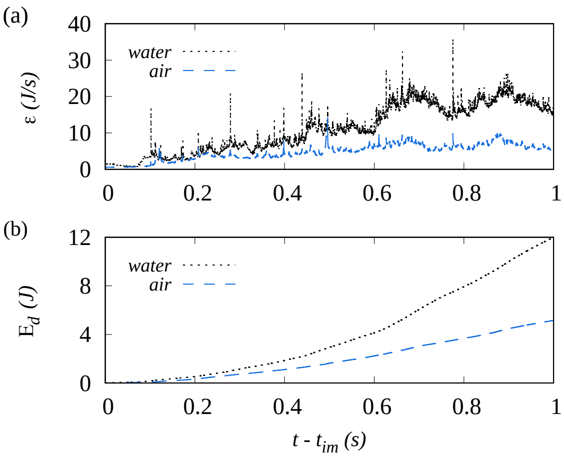

Figure 6. Time histories of the viscous dissipation rate ϵ (a) and corresponding dissipation E_{d} (b)

Figure 6. depicts the time histories of the viscous dissipation rate ϵ and the corresponding dissipation E_{d}. Since we compute breaking waves in a 2D simulation, we consider the width in the spanwise direction as a unit. The dissipation rates in both water and air are markedly intermittent and their fluctuations are strongly synchronized in time. We note that the occurrence of maximum dissipation rate fluctuations is closely related to the exchange time of energy transfer, i.e. the moments when E_{k} and E_{p} reach their extreme values. As breaking process develops, the dissipation rate in water increases greatly, while the dissipation rate in air remains stable (a). Splash-up productions generally occur at a period when the viscous dissipation gradient in water grows dramatically, the viscous dissipation in water continues to increase and no significant decrease in the dissipation rate is observed until $t - t_{\mathrm{im}} = 1s$. Most of the dissipation is caused by air in the early stage after breaking, and then water-induced dissipation dominates the energy dissipation due to the increasing dissipation rate in water (b).

4.3. Air Entrainment

Wave breaking injects a large amount of air into the water by the entrainment of bubbles, which is distinguished by a wide distribution of bubble sizes. The 2D numerical studies in the wave breaking literature may not able to investigate the accurate bubble size distributions, but the evolution of their formation and breakup processes can generally be captured on a fine grid scale through the DNS in this study. Figure 7. shows the time histories of the number of bubbles

$N(t)$ and the total area of bubbles ingested into the water normalized by the main cavity size A/A_0.

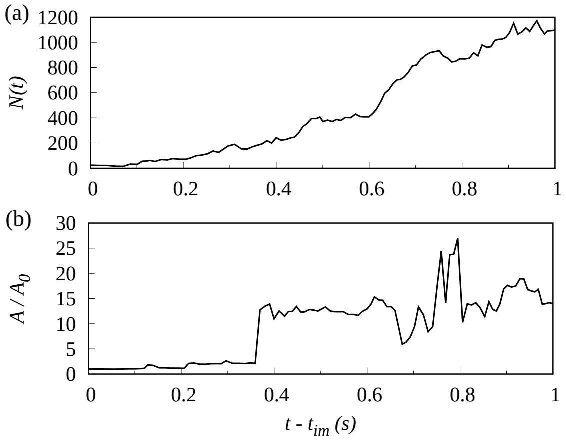

Figure 7. Time histories of the number of bubbles $N(t)$ (a) and the total area of bubbles normalized by the main cavity size A/A_0 (b)

The first bubble can be identified at the moment when the plunging jet impact on the wave front t_{im}, which is also referred to as the main cavity initially ingested in the breaking process. Subsequently, the first splash-up develops and penetrates into the water, with the main cavity being squeezed and distorted, generating a large number of small bubbles. During this period, the total number of bubbles $N(t)$ begins to increase, but the total ingested area of bubbles has no significant increase. Then the total ingested bubbles spikes to a higher size at around $t - t_{\mathrm{im}} = 0.37s$, this abrupt increase is associated with the behavior of the first splash-up impacting on and connecting to the free surface. A similar phenomenon occurs for the second splash-up at $t - t_{\mathrm{im}} = 0.67s$. It shows that the bubble size enclosed by the first and second splash-up is more than ten times larger than that of the main cavity. We also observe a transient collapse in the total ingested area of bubbles due to the intermittent rupture and reconnection of the ligaments on the top face of the splash-ups (b). As shown in Fig. 7(a), there is a roughly constant production rate at $0.1s$ that lasts until $0.6s$, and then the number of bubbles increases rapidly, which is related to the breakup of the main cavity due to turbulence around the cavity. It's worth noting that the temporal development of the number of bubbles shows a high similarity to the viscous dissipation rate during the breaking process, implying a possible link between the number of bubbles and the energy dissipation rate.

5. SUMMARY

We have presented 2D direct numerical simulations of breaking waves in shallow water generated by the wave plate using Basilisk to solve the two-phase Navier-Stokes equations with surface tension. High-fidelity modeling of experimental waves has been achieved by reconstructing the piston-type wave plate numerically to provide precise information on the hydrodynamics and energetics of the breakers as well as statistics on bubble productions. For the relationship between the changing maximum wave plate speed and the associated maximum wave height before breaking, we have investigated the onset of wave breaking in terms of the ratio of wave height to water depth, and determined critical values for the transitions between non-breaking wave, spilling breaker, and plunging breaker. For a typical plunging breaking wave with a large ratio of wave height to water depth, We obtain a good collapse of the free-surface profiles and entrapped air characteristics with respect to the experiment, showing the ability to resolve wave hydrodynamics and breaking processes over a large scale separation. We present a time-evolving energy budget to analyze the energy transfer and decay due to breaking, showing an intermittent and growing viscous dissipation rate induced by air-water mixture and vortical structures in the post-breaking stage. The corresponding relationship between bubble statistics and breaking processes has also been investigated, revealing a strong correlation between the number of bubbles and the energy dissipation rate.

ACKNOWLEDGEMENTS

This work has been supported by the scholarship from China Scholarship Council (CSC) under the Grant No. 201906090270. Computations were performed using computational resources on Advanced Research Computing (ARC) at Virginia Tech.

REFERENCES

[1] Duncan, J., 1981, "An experimental investigation of breaking waves produced by a towed hydrofoil", *Proceedings of the Royal Society of London A Mathematical and Physical Sciences*, Vol. 377 (1770), pp. 331–348.

[2] Melville, W., 1982, "The instability and breaking of deep-water waves", *Journal of Fluid Mechanics*, Vol. 115, pp. 165–185.

[3] Banner, M., and Peregrine, D., 1993, "Wave breaking in deep water", *Annual Review of Fluid Mechanics*, Vol. 25 (1), pp. 373–397.

[4] Melville, W. K., 1996, "The role of surface-wave breaking in air-sea interaction", *Annual review of fluid mechanics*, Vol. 28 (1), pp. 279–321.

[5] Perlin, M., Choi, W., and Tian, Z., 2013, "Breaking waves in deep and intermediate waters", *Annual review of fluid mechanics*, Vol. 45, pp. 115–145.

[6] Derakhti, M., Kirby, J. T., Banner, M. L., Grilli, S. T., and Thomson, J., 2020, "A unified breaking onset criterion for surface gravity water waves in arbitrary depth", *Journal of*

Geophysical Research: Oceans, Vol. 125 (7), p. e2019JC015886.

[7] Fuster, D., and Popinet, S., 2018, "An all-Mach method for the simulation of bubble dynamics problems in the presence of surface tension", *Journal of Computational Physics*, Vol. 374, pp. 752–768.

[8] Scardovelli, R., and Zaleski, S., 1999, "Direct numerical simulation of free-surface and interfacial flow", *Annual review of fluid mechanics*, Vol. 31 (1), pp. 567–603.

[9] Bell, J. B., Colella, P., and Glaz, H. M., 1989, "A second-order projection method for the incompressible Navier-Stokes equations", *Journal of computational physics*, Vol. 85 (2), pp. 257–283.

[10] Wroniszewski, P. A., Verschaeve, J. C., and Pedersen, G. K., 2014, "Benchmarking of Navier–Stokes codes for free surface simulations by means of a solitary wave", *Coastal Engineering*, Vol. 91, pp. 1–17.

[11] Hirt, C. W., and Nichols, B. D., 1981, "Volume of fluid (VOF) method for the dynamics of free boundaries", *Journal of computational physics*, Vol. 39 (1), pp. 201–225.

[12] Kothe, D. B., Mjolsness, R. C., and Torrey, M. D., 1991, *RIPPLE: A computer program for incompressible flows with free surfaces*, Available to DOE and DOE contractors from OSTI.

[13] Zhang, B., Popinet, S., and Ling, Y., 2020, "Modeling and detailed numerical simulation of the primary breakup of a gasoline surrogate jet under non-evaporative operating conditions", *International Journal of Multiphase Flow*, Vol. 130, p. 103362.

[14] Aulisa, E., Manservisi, S., Scardovelli, R., and Zaleski, S., 2007, "Interface reconstruction with least-squares fit and split advection in three-dimensional Cartesian geometry", *Journal of Computational Physics*, Vol. 225 (2), pp. 2301–2319.

[15] Scardovelli, R., and Zaleski, S., 2000, "Analytical relations connecting linear interfaces and volume fractions in rectangular grids", *Journal of Computational Physics*, Vol. 164 (1), pp. 228–237.

[16] Brackbill, J. U., Kothe, D. B., and Zemach, C., 1992, "A continuum method for modeling surface tension", *Journal of computational physics*, Vol. 100 (2), pp. 335–354.

[17] Francois, M. M., Cummins, S. J., Dendy, E. D., Kothe, D. B., Sicilian, J. M., and Williams, M. W., 2006, "A balanced-force algorithm for continuous and sharp interfacial surface tension models within a volume tracking framework", *Journal of Computational Physics*, Vol. 213 (1), pp. 141–173.

[18] Popinet, S., 2009, "An accurate adaptive solver for surface-tension-driven interfacial flows", *Journal of Computational Physics*, Vol. 228 (16), pp. 5838–5866.

[19] Popinet, S., 2018, "Numerical models of surface tension", *Annual Review of Fluid Mechanics*, Vol. 50, pp. 49–75.

[20] Li, C., 2017, "Dispersion of Oil Spills by Breaking Waves", Ph.D. thesis, Johns Hopkins University.

[21] Afshar-Mohajer, N., Li, C., Rule, A. M., Katz, J., and Koehler, K., 2018, "A laboratory study of particulate and gaseous emissions from crude oil and crude oil-dispersant contaminated seawater due to breaking waves", *Atmospheric Environment*, Vol. 179, pp. 177–186.

[22] Sumer, B. M., Jensen, P. M., Sørensen, L. B., Fredsøe, J., Liu, P. L.-F., and Carstensen, S., 2010, "Coherent structures in wave boundary layers. Part 2. Solitary motion", *Journal of fluid mechanics*, Vol. 646, pp. 207–231.

[23] Van Hooft, J. A., Popinet, S., Van Heerwaarden, C. C., Van der Linden, S. J., de Roode, S. R., and Van de Wiel, B. J., 2018, "Towards adaptive grids for atmospheric boundary-layer simulations", *Boundary-layer meteorology*, Vol. 167 (3), pp. 421–443.

[24] Mostert, W., and Deike, L., 2020, "Inertial energy dissipation in shallow-water breaking waves", *Journal of Fluid Mechanics*, Vol. 890.

[25] Wei, Z., Li, C., Dalrymple, R. A., Derakhti, M., and Katz, J., 2018, "Chaos in breaking waves", *Coastal Engineering*, Vol. 140, pp. 272–291.